NANOMATERIALS

Molecular templating of layered halide perovskite nanowires

Wenhao Shao[1]†, Jeong Hui Kim[1]†, Jeffrey Simon[2], Zhichen Nian[1], Sung-Doo Baek[1], Yuan Lu[3], Colton B. Fruhling[2], Hanjun Yang[1,4], Kang Wang[1,5], Jee Yung Park[1], Libai Huang[4], Yi Yu[3], Alexandra Boltasseva[2,6], Brett M. Savoie[1], Vladimir M. Shalaev[2,6], Letian Dou[1,4,6]*

Layered metal-halide perovskites, or two-dimensional perovskites, can be synthesized in solution, and their optical and electronic properties can be tuned by changing their composition. We report a molecular templating method that restricted crystal growth along all crystallographic directions except for [110] and promoted one-dimensional growth. Our approach is widely applicable to synthesize a range of high-quality layered perovskite nanowires with large aspect ratios and tunable organic-inorganic chemical compositions. These nanowires form exceptionally well-defined and flexible cavities that exhibited a wide range of unusual optical properties beyond those of conventional perovskite nanowires. We observed anisotropic emission polarization, low-loss waveguiding (below 3 decibels per millimeter), and efficient low-threshold light amplification (below 20 microjoules per square centimeter).

Layered metal-halide perovskites, or two-dimensional (2D) perovskites, can be synthesized in solution, and their optical and electronic properties can be tuned by changing their composition (*1*). Growth of 1D forms of these materials has been limited to vapor-phase growth (*2*, *3*) of $(BA)_2PbI_4$, where BA is butylammonium, or to lithographically templated solution-phase growth of $(BA)_2(MA)_{n-1}Pb_nI_{3n+1}$, where MA is methylammonium and the layer number n is 2 to 5 (*4*, *5*). These methods have high processing complexity and cost as well as limited scalability and design flexibility. Notably, the structure of layered perovskites has inspired the use of bulky organic spacers with engineered bandgaps (*6*, *7*) and intermolecular π interactions (*8*). We have found organic templating molecules that can break the in-plane symmetry of layered perovskites and induce 1D growth through secondary bonding interactions. Specifically, these molecules introduce in-plane hydrogen bonding that is compatible with both the ionic nature and octahedron spacing of halide perovskites. Nanowires of layered perovskites can be readily assembled in solution facilitated by the formation of a 1D H-bonded organic network. These nanowires with tailorable lengths and high-quality cavities provide an ideal platform to study anisotropic excitonic behaviors, light propagation, and lasing in layered perovskites. Our approach highlights the structural tunability of organic-inorganic hybrid semiconductors, which also brings unprecedented morphological control to layered materials.

[1]Davidson School of Chemical Engineering, Purdue University, West Lafayette, IN 47907, USA. [2]Elmore Family School of Electrical and Computer Engineering, Purdue University, West Lafayette, IN 47907, USA. [3]School of Physical Science and Technology and Shanghai Key Laboratory of High-resolution Electron Microscopy, ShanghaiTech University, Shanghai 201210, China. [4]Department of Chemistry, Purdue University, West Lafayette, IN 47907, USA. [5]Key Laboratory of Photochemistry, Institute of Chemistry, Chinese Academy of Sciences, Beijing 100190, China. [6]Birck Nanotechnology Center, Purdue University, West Lafayette, IN 47907, USA.
*Corresponding author. Email: dou10@purdue.edu
†These authors contributed equally to this work.

In-plane unidirectional H bonding

Organic spacers for layered perovskites typically impose weak long-range order. For example, an out-of-plane view along the stacking direction of $(PEA)_2PbBr_4$, where PEA is phenylethylammonium, shows weak intermolecular interactions in the organic layer (Fig. 1A). To align the cations, carboxylic acid (COOH) was chosen to dimerize through multiple H bonds, which have strong directionality and are widely used to drive the self-assembly and alignment of organic building blocks (*9*). Derivatizing PEA with COOH to the 3-position of the phenyl ring resulted in the out-of-plane formation of classic COOH dimers across the van der Waals gap (Fig. 1B), as previously observed in 2D perovskites (*10*). However, this out-of-plane directionality did not alter the in-plane growth of layered perovskite crystals, and only 2D nanostructures were obtained.

To direct 1D growth, we first attempted to align the H bonds parallel to inorganic slabs. An additional COOH unit was introduced in the para position of the existing moiety to form a backbone resembling terephthalic acid (TPA), that we named TPA3 [2-(2,5-dicarboxyphenoxy)ethan-1-aminium; Fig. 1C]. The crystal structure of $(TPA3)_2PbBr_4$ revealed well-aligned, parallel 1D chains of TPA3 on top of 2D inorganic slabs driven by unidirectional intermolecular interactions (Fig. 1, C and E). Adjacent TPA moieties were connected along the [010] crystallographic direction with a spacing of 9.54 Å characterized by the aromatic centroid distance. Each 1D chain consisted of periodic COOH dimers with an average H-bonding distance of 1.78 Å.

This unidirectional in-plane connectivit the organic layer led to the solution-phase assembly of layered perovskites exclusively into needles and wires (Fig. 1C and fig. S1). These 1D crystals had a mean aspect ratio as large as 28.9 (fig. S2). However, the TPA3-based structures exhibited several unsatisfactory morphological and optical properties. Growing high-quality crystals (fig. S3, A and B) required a very slow self-assembly process because fast growth usually led to poorly defined end facets (Fig. 1C and fig. S3, D to H) or even hyperbranched crystals, as observed in the case of $(TPA3)_2PbI_4$ (fig. S4, A and B, and movie S1). Negligible excitonic features were observed even from photoluminescence (PL) of slow-assembled $(TPA3)_2PbBr_4$ single crystals. The emission was dominated by a broad band that we attributed to self-trapped excitons or in-gap defect states (fig. S3, B and C) (*11*). The iodide counterpart instead presented broad excitonic emission (fig. S4, C to E). We hypothesized that strong H bonds disrupted the assembly of ionic species and led to extensive defect formation during crystal growth that drove hyperbranching. Considerable octahedral distortion was observed in $(TPA3)_2PbBr_4$ (characterized by the Pb-Br bond distance variation, $\Delta d = 9.1 \times 10^{-4}$; Fig. 1E) that was associated with quenched excitonic feature and broadband emission (*12*).

Partially broken 1D chains

To balance secondary bonding with ionic assembly, we partially disrupted the 1D H-bonding network by substituting one COOH unit in the TPA backbone with bromine, which prevented COOH dimers from twisting back to form out-of-plane H bonds. This candidate, BrCA3 [2-(2-bromo-5-carboxyphenoxy)ethan-1-aminium] maintained a similar in-plane connectivity but formed parallelly aligned "partially broken" 1D chains above inorganic slabs (Fig. 1D), which were parallel to the $[3\bar{1}0]$ direction but deviated from the stacking directions of the octahedrons. Octahedral distortions were reduced by an order of magnitude ($\Delta d = 8.9 \times 10^{-5}$), presumably from the relief of stress in the H-bonded network. Each chain was constructed by pairs of BrCA3 through COOH dimerization with the same spacing and H-bonding distance as those in the TPA3 counterpart. Adjacent molecules were well separated at the bromine terminal, with an intermolecular Br-Br spacing of 3.30 Å (Fig. 1F), and allowed the occupation of water molecules stabilized through H bonding with ammonium tails. Given the hygroscopic nature of halide perovskites, this partial occupancy of water is rather unusual.

The partially broken 1D connectivity introduced by BrCA3 promoted balanced and rapid 1D self-assembly of layered perovskites. Crystal growth was further accelerated at the droplet-air interface to produce high-quality nanowires. This floating growth method was originally developed (*13*) for capturing thin 2D sheets of

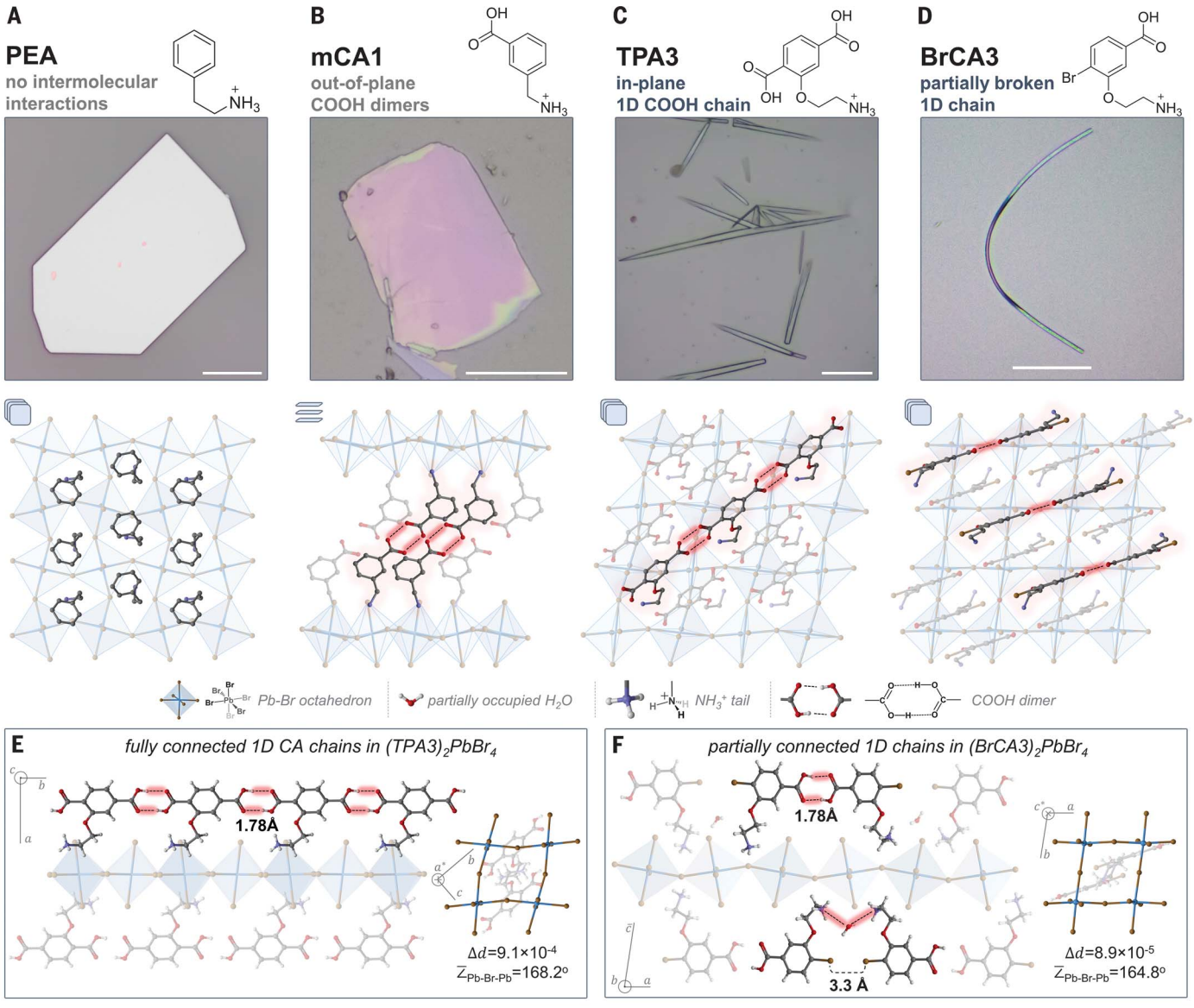

Fig. 1. A comparison among the morphology and crystal structures of layered $[PbBr_4]^{2-}$ perovskites based on various organic cations. (**A**) PEA, phenylethylammonium. (**B**) mCA1, (3-carboxyphenyl)methanaminium. (**C**) TPA3, 2-(2,5-dicarboxyphenoxy)ethan-1-aminium. (**D**) BrCA3, 2-(2-bromo-5-carboxyphenoxy)ethan-1-aminium. The middle panels show the morphology of each crystal obtained with the floating growth method under a bright-field optical microscope (scale bars, 20 μm). Bottom panels highlight the alignment of cations viewed along stacking directions, except in $(mCA1)_2PbBr_4$, which was viewed perpendicular to the stacking direction because of the out-of-plane COOH dimers. H atoms are omitted for clarity. (**E** and **F**) Examinations of the 1D H-bonding chains in $(TPA3)_2PbBr_4$ (E) and $(BrCA3)_2PbBr_4$ (F) along with illustrations of octahedral distortion and lattice tilting, characterized by Pb-Br bond distance variation (Δd) and average Pb-Br-Pb angle ($\bar{\angle}_{Pb-Br-Pb}$), respectively. Despite similar $\bar{\angle}_{Pb-Br-Pb}$, Δd was reduced by an order of magnitude in $(BrCA3)_2PbBr_4$. Room-temperature crystal structures were used throughout this article, and all illustrations are based on actual crystal structures.

layered perovskites and subsequent transfer preserving pristine morphology (materials and methods). The nucleation and 1D growth of $(BrCA3)_2PbBr_4$ were studied with in situ microscopy (movie S2) revealing a growth rate that was ~40 times as fast along the long axis compared with the short (fig. S5). Nanowires of $(BrCA3)_2PbBr_4$ exhibited a mean length, width, and height of 8.45 μm, 409 nm, and 361 nm, respectively, and maintained a mean aspect ratio of 22.0 (fig. S6). A characteristic nanowire shown in Fig. 1D had an exceptional aspect ratio of >100 (~80 μm long and ~0.7 μm wide), well-defined end facets, and a twisted morphology. The solution-phase synthesis additionally allowed easy scaling-up, cleaning, and surface coating of nanowires with dense and uniform coverage (materials and methods and fig. S7).

Growth mechanism studies

Although the formation of 2D perovskite nanowires appeared to depend on the inherent 1D connectivity within the organic layer, additional studies were needed to determine whether their growth direction followed the H-bond direction of COOH dimers. We used single-crystal x-ray diffraction (SC-XRD) and selected-area electron diffraction (SAED) to face-index bulk crystals and nanowires of $(BrCA3)_2PbBr_4$, respectively (Fig. 2, A to C, and fig. S8). The long axis of each crystal was aligned with its [110] crystallographic direction and the short axis with $[1\bar{1}0]$, both matching the octahedron stacking direction. However, the COOH dimers (along $[3\bar{1}0]$) were at an angle of 63° relative to the [110] long axis, and the dimer orientation in

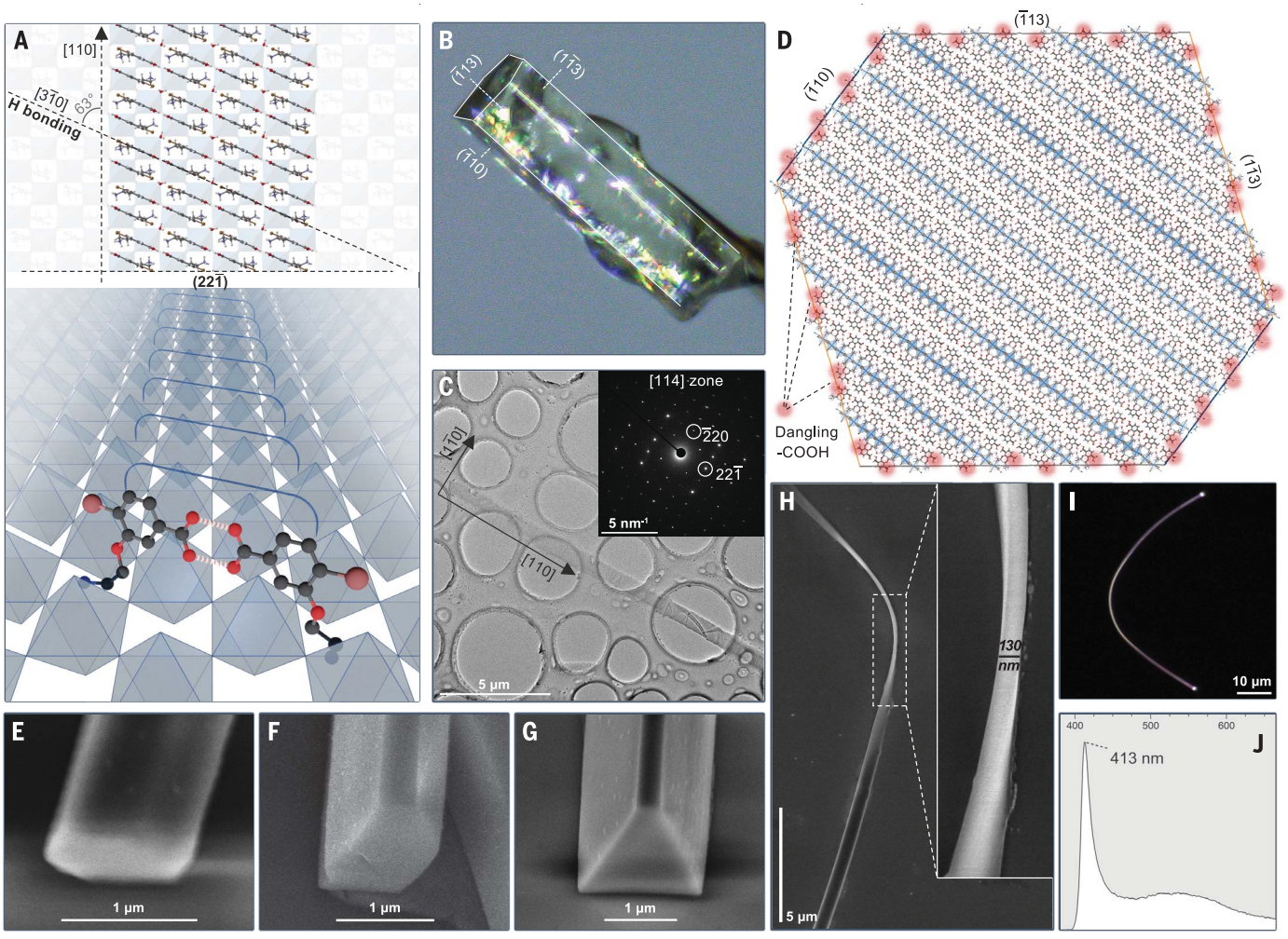

Fig. 2. Growth mechanism of 2D perovskite nanowires illustrated with $(BrCA3)_2PbBr_4$ and morphological and optical properties. (**A**) Stacking plane cross-sectional view. The 3D model (below) intuitively illustrates the molecular templating effect, involving pairs of BrCA3 dimers sitting on an inorganic slab. (**B**) A hexagonal cylindrical bulk crystal with side facets indexed as $(\bar{1}10)$, $(\bar{1}13)$, and $(1\bar{1}3)$ by SC-XRD and their Friedel pairs. More examples are shown in fig. S8. (**C**) TEM images of a nanowire and its SAED pattern (inset) viewed along zone axis [114] showing the growth along [110]. (**D**) Cross-sectional view of the $(22\bar{1})$ end facet along [110]. The three pairs of facets indexed in (B) are marked. Red clouds represent the surface dangling COOH. All six facets exhibit pronounced coverage and protection by COOH. (**E** to **G**) Nanowire end facet morphology under scanning electron microscopy (SEM). (**H**) A 180°-twisted nanoribbon under SEM. (**I** and **J**) PL image (I) and spectrum (J) of the twisted nanowire presented in Fig. 1D, showing white emission.

the TPA3 counterpart was perpendicular to its long axis (fig. S9). These findings contradicted our initial intuitive hypothesis that nanowires would grow along the directional H bonds.

Instead, the COOH dimers hindered rather than facilitated the growth of layered perovskites. Alignment of cations correlated with the distinct exposure of COOH moieties at the side versus the end facets (here, side facets refer to all of the facets parallel to the long axis), as shown in Fig. 2D for the $(22\bar{1})$ end facet when viewed along the [110] growth direction. Six side facets were subsequently indexed as $(\bar{1}10)$, $(\bar{1}13)$, $(1\bar{1}3)$, and their Friedel pairs according to the hexagonal cylindrical crystal previously investigated with SC-XRD (Fig. 2B and fig. S8A). Dangling COOH moieties were abundant on all six side facets (Fig. 2D) because of the near-perpendicular H-bond alignment with the long axis, [110]. Notably absent was the (001) facet parallel to the $[PbBr_4]^{2-}$ slabs, which was typically observed in conventional 2D perovskites but instead subdivided into $(\bar{1}13)$ and $(1\bar{1}3)$, which further enhanced the surface exposure of COOH.

These findings suggested that surface dangling carboxylic acids would slow down crystal growth and lead to the preferred exposure of COOH-abundant surfaces. In previously reported polymer-assisted synthesis of oxide perovskite $Pb(Zr/Ti)O_3$ nanowires (*14*), the polymer was hypothesized to reduce the surface tension of certain crystallographic planes. Nanowire growth was thus driven by the coverage of high-energy exposed surfaces and left them as end facets. In our system, surface dangling carboxylic acids protected nanowire side facets by forming robust H bonds with water, and incoming cations must break the existing solvent shield. In fact, water was an essential solvent for 1D growth: Crystals randomly nucleated and clustered in nonaqueous media even within protic alcohols (fig. S10). Water passivation lowered the surface energy of COOH-abundant facets, but such an effect became particularly weak at the $(22\bar{1})$ end. As illustrated in fig. S11, the $(\bar{1}10)$ side facets were uniformly covered with dangling COOH moieties, whereas the density was nearly halved at $(22\bar{1})$, which was insufficient to protect it from incoming cations. Surface energies of notable facets calculated with density functional theory (DFT) revealed considerable anisotropy after addressing the effects from

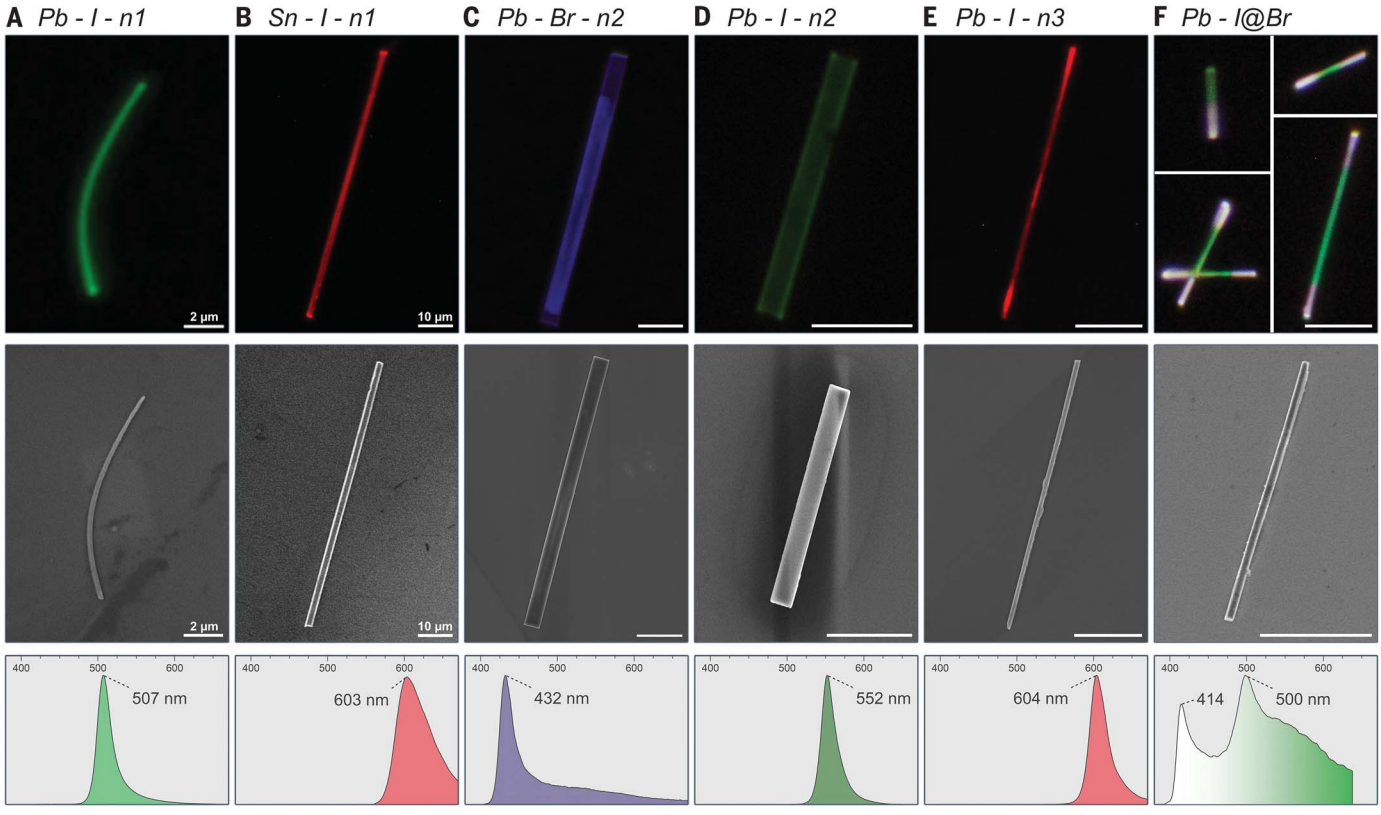

Fig. 3. The expanded library of layered 2D and quasi-2D perovskite nanowires. (**A**) $(BrCA3)_2PbI_4$. (**B**) $(BrCA3)_2SnI_4$. (**C**) $(BrCA3)_2MAPb_2Br_7$ (n = 2). (**D**) $(BrCA3)_2MAPb_2I_7$ (n = 2). (**E**) $(BrCA3)_2MA_2Pb_3I_{10}$ (n = 3). PL images (top), SEM images (middle), and PL spectra (bottom) of each candidate are included. (**F**) Longitudinal epitaxial heterostructures grown with the $(BrCA3)_2PbI_4$ core and bromide shell. The SEM image (middle) shows negligible trace of core-shell interfaces, in contrast to the easily distinguishable Br-I interface from the PL images above. Scale bars, 2 μm in (A) and 10 μm in (B) to (F).

water passivation, leading to higher surface energy at the $(22\bar{1})$ facet (fig. S11, F and G).

Thus, the molecular templating effect of in-plane COOH dimers aligned organic cations and drove the anisotropic surface termination of dangling COOH moieties that protected these surfaces through robust H bonding with aqueous solvent molecules. The discussions spanning crystal nucleation, molecular and unit cell level, nanowire morphology, and bulk crystals were integrated in fig. S12 and supplementary text 1. In particular, this mechanism points to the crucial alignment of H bonds with the growth direction (90° in TPA3 and 63° in BrCA3-templated counterparts), which affected the relative abundance of dangling COOH on side versus end facets and therefore the effect of 1D growth. A perfect perpendicular alignment in $(TPA3)_2PbBr_4$ led to rapid 1D growth but poor cavities in nanocrystals, whereas the seemingly imperfect H-bond alignment in $(BrCA3)_2PbBr_4$ presented a well-balanced crystal growth and nanowires with excellent cavities.

Nanowires of $(BrCA3)_2PbBr_4$ displayed diverse morphologies that were commonly observed with hexagonal or acute trapezoidal end facets (Fig. 2, E to G). The interplay among side facets could lead to distinct termination morphology even within a single nanowire (fig. S13A). These intricate morphological features likely stem from the surface modification with dangling COOH, so a range of low-energy facets were exposed. Notably, narrow and thin crystals (~30 nm) also exhibited smooth terminations (fig. S13B). They easily bend or twist; Fig. 2G shows 180° twisting of a nanoribbon. High-resolution transmission electron microscopy (TEM) provided additional structural characterizations despite the high sensitivity of 2D perovskite nanowires to electron beam damage (fig. S14). Optically, $(BrCA3)_2PbBr_4$ exhibited white PL at room temperature with a sharp excitonic peak at 413 nm and lower-energy broad emission band (Fig. 2, I and J). The PL characteristics were unaffected by bending or twisting.

An expanded library of layered perovskite nanowires

We used the BrCA3 spacer to synthesize a wide range of layered perovskites. For example, BrCA3-based nanowires with $[PbI_4]^{2-}$ and $[SnI_4]^{2-}$ matrices were readily obtained (Fig. 3, A and B). These candidates exhibited better stability against ambience, heat, and light compared with PEA-based structures (figs. S15 to S17). High aspect ratios were generally achievable in quasi-2D perovskites, such as n = 2 $(BrCA3)_2MAPb_2Br_7$ (Fig. 3C) and n = 2 and n = 3 in lead-iodide counterparts (Fig. 3, D and E). Epitaxial growth of these nanowires originated from their end facets. Representative diblock or triblock longitudinal heterostructures obtained with deliberate fast nucleation of $(BrCA3)_2PbBr_4$ on the as-grown iodide cores (materials and methods) had interfaces between the core and shell that were morphologically indiscernible (Fig. 3F), but the longitudinal extension of bromide segments could be distinguished by its distinctive white PL. Coaxial growth around the side facets of iodide cores remained negligible because dangling COOH groups on each side facet shielded as-grown crystals against the coaxial nucleation of additional layers. Enhanced core and shell resolution was further achieved through selectively exciting bromide or iodide sections (fig. S18, A to E). In contrast to those synthesized with 3D halide perovskites with a gradient ion distribution (*15*), nanowire heterostructures based on layered perovskites had enhanced stability against halide migration that preserved Br-I interface contrast (fig. S18F).

The use of partially broken 1D H-bonded chain was expanded by substituting bromide groups in BrCA3 with fluoride or methyl groups. These derivatives also enabled 1D growth of layered perovskite nanowires (fig. S19). Optically, compared with $(BrCA3)_2PbBr_4$, the emission was yellowish green for the methyl analog but bluish white for the fluoride analog. Although broadband emission reduced the color purity, it also facilitated color tunability in layered perovskite nanowires with subtle variation of organic spacers.

Unusual optical properties

Morphologically restricting the growth of layered perovskites into 1D nanowires led to distinctive optical properties along, perpendicular, or both to the stacking direction of these layered structures. Emission typically displayed weak linear polarization [degree of polarization (DOP) < 3%] with propagation direction approximately along their long axes (fig. S20), which we attributed to the anisotropic confinement of electric field within high–aspect ratio nanostructures (*16*). However, a 58% DOP was observed from a representative candidate of $(BrCA3)_2PbI_4$ (Fig. 4A), where the emission propagated almost perpendicular to its long axis, in contradiction with our previous observations.

Layered perovskites exhibited intrinsic emission polarization caused by the in-plane confinement of excitons (*17*). Such a phenomenon is challenging to observe in 2D plates when viewed along the stacking direction in a typical epidetection setup, whereas nanowires offer accessibility to their side facets. Therefore, when viewing perpendicular to the stacking direction, strong linearly polarized PL was revealed that propagated perpendicular to the long axes, which could explain the observation in Fig. 4A.

We examined a piece of twisted $(BrCA3)_2PbI_4$ nanowire to resolve the origin of its polarization dependence (Fig. 4B). Twisting allowed the observation of both in-plane and out-of-plane optical properties within a single nanowire. As illustrated subsequently, inorganic slabs were originally stacked parallel to the substrate on the top of the image, and then crystal gradually twisted to allow the view perpendicular to its stacking direction. The twisting action allowed the observation of diverse polarization profile within the same crystal, which was further quantified and spatially resolved. Emission polarization was negligible at the top, but the crystal gradually exhibited linearly polarized emission with slowly rotated polarization direction along the twisting action, resulting in a DOP of 40% at the bottom. This demonstration of twist-dependent tunable emission polarization from a single semiconductor nanowire arose from the combination of layered crystal structure, 1D growth kinetics, and the twisted morphology.

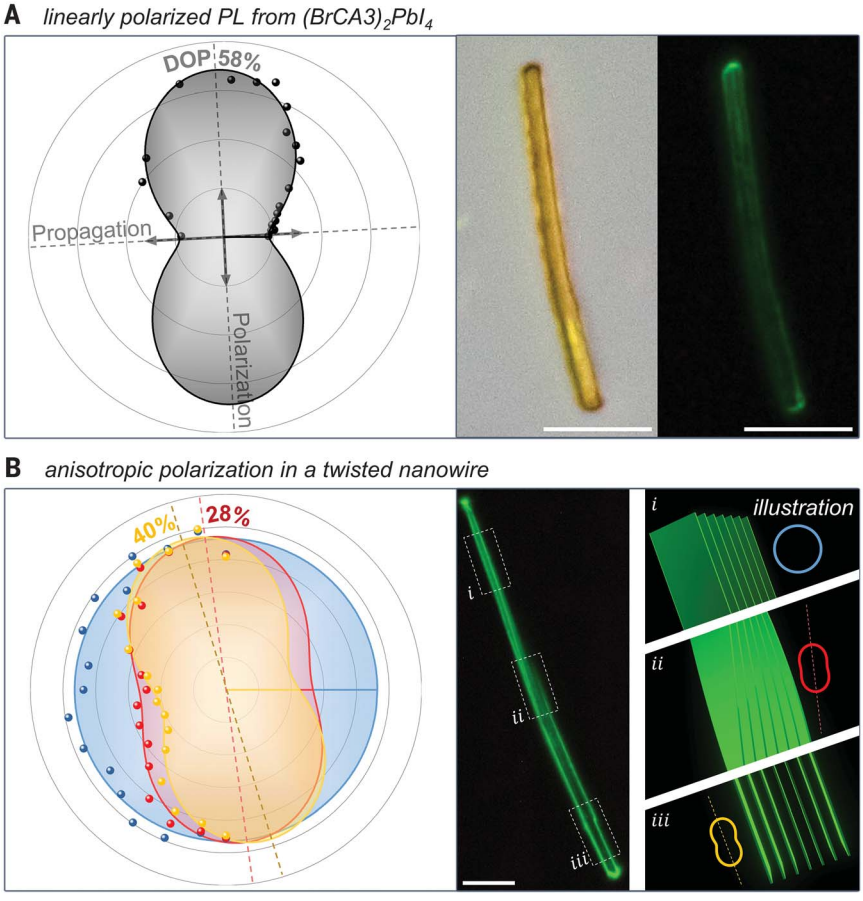

Fig. 4. Anisotropic emission polarization. (**A**) Linearly polarized PL detected from a nanowire of $(BrCA3)_2PbI_4$ with a high DOP of 58% and PL propagated almost perpendicular to the long axis. (**B**) The mechanism was revealed from a twisted nanowire showing strong emission polarization only when viewed perpendicular to its stacking direction (bottom). This twisted crystal is modeled on the right, where the blue circle and the red and yellow peanut shapes are exact extracts from the polar graph (left), showing the varying polarization profile along the twisting action with a DOP of 28% (red, section ii) and 40% (yellow, section iii). Scale bars, 10 μm.

Nanowires of layered perovskites are candidates for active waveguides given their tailorable length, emission tunability, and flexibility. Waveguide losses were assessed from several ~100-μm-long wires of $(BrCA3)_2PbBr_4$ according to their propagation distance–dependent relative tip emission intensity collected and analyzed with far-field PL images (materials and methods). Nanowires of $(BrCA3)_2PbBr_4$ exhibited intrinsic loss coefficients as low as 2.7 dB/mm, as observed in straight samples (Fig. 5A). Best-performing contemporary inorganic (*18*, *19*) and organic (*20*) semiconductor waveguides typically exhibit losses within 10 dB/mm. Narrow and bent nanowires (Fig. 5B), or even strongly twisted ones (Fig. 5C), had similar losses to those of wide and straight waveguides as they remained crystalline after bending or twisting.

Waveguides could be coupled to transport light to adjacent crystals and create a complex optical network (*18*). A few coupled nanowires were examined through tip-tip interactions or cross-intersections (Fig. 5D and fig. S21), demonstrating proof-of-concept potentials to construct more-complex optical networks. Directional propagation of light within 1D nanowires was necessary to ensure efficient coupling of waveguides. Figure 5D shows a perpendicular pair of cross-coupled waveguides that formed multiple scattering sites. Because of the 1D propagation of light, only the right end of the intersection could be illuminated when excitation light was injected from the left side of the intersection, and vice versa. Minimal outcoupled light was detected from the vertical nanowire when the horizontal crystal was excited.

Building on previous studies of semiconductor nanowire lasers (*21*) and lasing in 3D halide perovskites (*22*, *23*), we investigated the light amplification behavior of BrCA3-based nanowires. In lead-based layered perovskites, the lasing threshold is often constrained by the strong exciton-phonon interaction or Auger recombination (*7*). Enhanced lasing performances

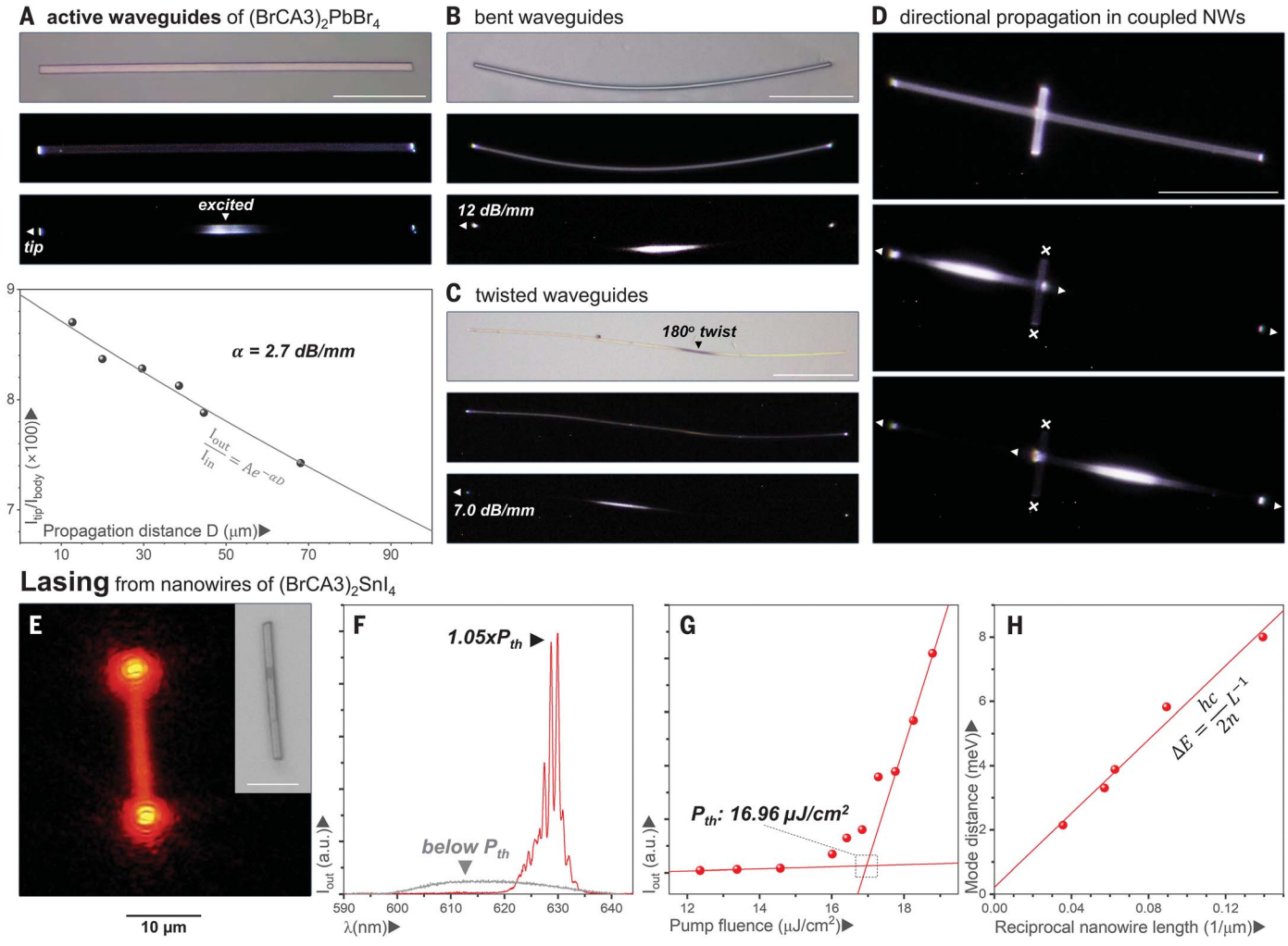

Fig. 5. Waveguiding and lasing. (**A**) Intrinsic loss coefficients measured from a straight nanowire of $(BrCA3)_2PbBr_4$ and extracted from the plot (bottom) of propagation distance–dependent relative tip emission intensity. (**B** and **C**) Bent (B) and twisted (C) nanowires were examined, showing low loss coefficients as well. (**D**) A pair of cross-coupled nanowires (NWs) excited at the horizontal waveguide from left or right of the intersection. (**E**) A representative nanowire of $(BrCA3)_2SnI_4$ pumped above the threshold at 88 K, showing majority emission from the two end facets with coherent interference patterns. (Inset) Grayscale brightfield image. (**F**) Emission spectra of the stimulated lasing (red) versus the spontaneous emission (gray). a.u., arbitrary units. (**G**) Threshold response examined from integrated outcoupled emission plotted against the pump fluence. (**H**) Mode distance against the reciprocal nanowire length examined from a series of lasing nanowires, which was fitted according to Fabry-Perot modes. Scale bars, 20 μm.

have been pursued in quasi-2D systems (*24*, *25*). Tin-based 2D perovskites may exhibit lasing performances surpassing those of their lead counterparts, as has been shown in recent studies (*26*). However, their lasing thresholds are still in the ~100-μJ/cm^2 regime with substantial sample-to-sample variation; both limitations arise from the lack of a well-established cavity. Temperature-dependent and time-resolved PL studies comparing $(BrCA3)_2SnI_4$ and $(BrCA3)_2PbI_4$ revealed higher exciton-phonon coupling and contribution from self-trapped excitons or defect states in the lead counterpart (figs. S22 and S23), both of which are not conducive to efficient lasing.

Emission from the two end facets in nanowires of $(BrCA3)_2SnI_4$ gradually became dominant with increasing pump fluence (fig. S24) and was accompanied by the appearance of spatial interference patterns (Fig. 5E) and multimode lasing at the lower-energy side of the spontaneous emission band (Fig. 5F). We monitored the integrated emission intensity across the threshold to determine a lasing threshold of 17 μJ/cm^2 (Fig. 5G) versus that of ~100 μJ/cm^2 observed in contemporary tin-based layered perovskites. The bright localized emission from the tips and multimode lasing from this ~16.0-μm-long nanowire were both consistent from the strong waveguiding behavior under Fabry-Perot modes. Mode spacing (ΔE) from a series of nanowires with varying lengths (L) decreased with L and followed a linear trend with the reciprocal nanowire length ($1/L$), confirming the Fabry-Perot cavity characteristics (Fig. 5H and fig. S25).

Discussion

The method to manipulate the morphology of layered perovskites by introducing robust intermolecular interactions between organic spacers is distinctive to the special crystal structures of organic-inorganic hybrid materials and requires more comprehensive investigations. In our implementation, the COOH dimer was originally exploited to enforce 1D connectivity within the organic layer. Unexpectedly, this directionality was transferred to the assembled system. Through a thorough examination, the molecular templating effect was elucidated as aligning spacers using in-plane directional H bonds, which further drove the anisotropic surface termination of dangling COOH that protected these facets through robust H bonds with aqueous solvent molecules.

Subsequently, balanced growth conditions and high-quality nanowires were achieved through subtle yet crucial manipulation over the alignment of H bonds with respect to growth direction. 2D perovskite nanowires based on BrCA3 incited a range of unusual optical properties. The intrinsic excitonic nature of layered halide perovskites enabled facile observation and control of polarized emission. These nanowires also revealed exceptional cavity qualities, which could be used as active waveguides with low propagation loss coefficients and to facilitate light amplification with low thresholds compared with other systems.

Morphological control with directional supramolecular synthons proves to be a generally applicable strategy for various layered perovskite structures and diverse organic spacers. However, its merit extends to a broad range of organic-inorganic hybrid materials. Particularly, the selection of functional groups and intermolecular interactions to be incorporated within the organic layer transcends far beyond COOH dimers and the H-bonding network. For example, π interactions (π-π, π-p, or σ-π), electrostatic forces, and even chirality could also be readily implemented (*8*). Further explorations in this regard will introduce enhanced versatility in these hybrid layered materials as the next-generation semiconductors, where the collective benefits of conventional organic and inorganic counterparts readily converge.

REFERENCES AND NOTES

1. B. Saparov, D. B. Mitzi, *Chem. Rev.* **116**, 4558–4596 (2016).
2. D. Ghoshal *et al*., *Adv. Opt. Mater.* **7**, 1900039 (2019).
3. P. Yadav *et al*., *Chem. Mater.* **35**, 3300–3306 (2023).
4. Y. Zhao *et al*., *J. Am. Chem. Soc.* **143**, 8437–8445 (2021).
5. J. Feng *et al*., *Nat. Electron.* **1**, 404–410 (2018).
6. Y. Gao *et al*., *Nat. Chem.* **11**, 1151–1157 (2019).
7. W. Shao, S. Yang, K. Wang, L. Dou, *J. Phys. Chem. Lett.* **14**, 2034–2046 (2023).
8. L. Yan, C. J. Gloor, A. M. Moran, W. You, *Appl. Phys. Lett.* **122**, 240501 (2023).
9. G. R. Desiraju, *Angew. Chem. Int. Ed.* **34**, 2311–2327 (1995).
10. M. B. AlShammari *et al*., *Chem. Phys. Lett.* **702**, 8–15 (2018).
11. S. Kahmann, E. K. Tekelenburg, H. Duim, M. E. Kamminga, M. A. Loi, *Nat. Commun.* **11**, 2344 (2020).
12. L. Mao, Y. Wu, C. C. Stoumpos, M. R. Wasielewski, M. G. Kanatzidis, *J. Am. Chem. Soc.* **139**, 5210–5215 (2017).
13. D. Pan *et al*., *Nat. Nanotechnol.* **16**, 159–165 (2021).
14. G. Xu *et al*., *Adv. Mater.* **17**, 907–910 (2005).
15. Y. Wang *et al*., *ACS Nano* **11**, 3355–3364 (2017).
16. J. Wang, M. S. Gudiksen, X. Duan, Y. Cui, C. M. Lieber, *Science* **293**, 1455–1457 (2001).
17. M. Wang, Z. Yang, C. Zhang, *Adv. Opt. Mater.* **9**, 2002236 (2021).
18. M. Law *et al*., *Science* **305**, 1269–1273 (2004).
19. X. Wang *et al*., *Science* **381**, 784–790 (2023).
20. Y. Li *et al*., *ACS Appl. Mater. Interfaces* **9**, 8910–8918 (2017).
21. M. H. Huang *et al*., *Science* **292**, 1897–1899 (2001).
22. G. Xing *et al*., *Nat. Mater.* **13**, 476–480 (2014).
23. H. Zhu *et al*., *Nat. Mater.* **14**, 636–642 (2015).
24. H. Zhang *et al*., *Angew. Chem. Int. Ed.* **57**, 7748–7752 (2018).
25. J. Y. Park *et al*., *Nat. Chem.* **15**, 1745–1753 (2023).
26. Y. Li *et al*., *Sci. Adv.* **9**, eadh0517 (2023).

ACKNOWLEDGMENTS

The authors acknowledge Y. H. Lee and his investigations on nanowire morphology under SEM, S. Zhang and the inspirations from him on crystal growth and data interpretations, M. Zeller for single-crystal data collection and refinement, C. Yuan for confocal laser scanning microscopy setup, and Q. Tu (Texas A&M) for the valuable discussions on crystal growth. **Funding:** This work is primarily supported by the US Department of Energy (DOE), Office of Basic Energy Sciences, under award no. DE-SC0022082 and by the US National Science Foundation under award nos. 2143568-DMR and 2110706-DMR. Z.N. and B.M.S. acknowledge support from the US DOE, Office of Energy Efficiency & Renewable Energy, under award no. DE-EE0009519. Y.Y. and Y.L. acknowledge support from the National Natural Science Foundation of China under award no. 52222311 and support from the Center for high-resolution Electron Microscopy (ChEM) at ShanghaiTech University. J.S., C.B.F., A.B., and V.M.S. acknowledge support from the US Office of Naval Research under award no. N00014-21-1-2026 and the US Air Force Office of Scientific Research through award no. FA9550-20-1-0124. J.S. also acknowledges the National Science Foundation Graduate Research Fellowship under grant no. DGE-1842166. H.Y. acknowledges financial support from the Lillian Gilbreth Postdoc Fellowship by the College of Engineering of Purdue University. The views expressed herein do not necessarily represent the views of the US DOE, the National Science Foundation, or the US government. **Author contributions:** Conceptualization: W.S. and L.D. Crystal growth methodology: W.S. and J.H.K. Lasing: W.S., J.S., C.B.F., A.B., and V.M.S. Computation: Z.N., W.S., and B.M.S. SEM: S.-D.B. and W.S. TEM: Y.L. and Y.Y. Material stability investigation: J.Y.P. Temperature variant PL and TRPL: H.Y. and L.H. Writing – original draft: W.S. Writing – review & editing: W.S., J.H.K., H.Y., K.W., C.B.F., A.B., B.M.S., and L.D. Supervision: L.D. **Competing interests:** L.D. and W.S. have filed a patent disclosure related to the nanowire synthesis. The other coauthors declare that they have no competing interests. **Data and materials availability:** All crystallographic data have been deposited in the Cambridge Crystallographic Data Centre (CCDC) database, with reference numbers 2292512 to 2292519 and 2295157. Other data are available in the main text or the supplementary materials.

SUPPLEMENTARY MATERIALS

science.org/doi/10.1126/science.adl0920
Materials and Methods
Supplementary Text
Figs. S1 to S27
Tables S1 to S11
NMR Spectra
References (*27*–*46*)
Movies S1 and S2

Submitted 1 October 2023; accepted 18 April 2024
10.1126/science.adl0920